ISSN 2029-6991 / eISSN 2029-7009

VILNIUS TECH
Vilnius Gediminas Technical University

GEODESY and CARTOGRAPHY

2024
Volume 50
Issue 2
Pages 104–112
https://doi.org/10.3846/gac.2024.18264

UDC 528.873

INFLUENCE OF NOISE EQUIVALENT BETA NAUGHT ESTIMATION ON BACKSCATTERING IMAGE CLASSIFICATION OF TERRASAR-X

Sumaya Falih HASAN[1], Muntadher Aidi SHAREEF[1]✉, Hussein Sabah JABER[2]

[1]*Department of Surveying Engineering Techniques, Technical College of Kirkuk, Northern Technical University, Kirkuk, Iraq*
[2]*Department of Surveying Engineering, College of Engineering, University of Baghdad, Baghdad, Iraq*

Article History:
- received 09 December 2022
- accepted 29 August 2024

Abstract. Noise Equivalent Beta Naught is the different noise influence that beneficence to the radar signal. This type of noise is available in TerraSAR-X satellite images and expressed in forms of scaled polynomial described the noise power. On the other hand, Sigma naught or backscattering coefficient represents the average reflectivity of a horizontal material samples which used to reflect the nature of the land use and land cover in radar images. In this paper, radar satellite images in dual VV and HH polarization were used to study the influence of the noise on backscattering image classification. The result demonstrated that the visual interpretation of sigma naught which is result from the comparison between existence case and absence case (in the other word: with and without noise) of the noise illustrated that there is no different between them. In the other hand, for more details and more precise, an example of small images are used to show the values of obtained backscattering. The result demonstrated that the NEBN plays the main roles in decreasing the values of backscattering coefficient in TSX image. The influence of this noise had usually high in water body surface, because this surface is generally having small backscattering coefficients compared with land cover.

Keywords: Noise Equivalent Beta Naught, TerraSAR-X, Strip map image, dual polarization.

✉Corresponding author. E-mail: ***muntadher.a.shareef@ntu.edu.iq***

1. Introduction

In essence, satellite images are digitally captured and then processed by computers to create images for a variety of features. The effectiveness of the used sensors as well as the development of the analysis and application-specific products will affect the computer process. However, due to the poor quality of the images, processing methods had to be developed in order to make the photographs useable (Mohammed Noori et al., 2018). Image restoration and correction, enhancement, and information extraction are the three main categories under which all satellite image processing activities can be divided (Rasti et al., 2022). Additionally, first category deals with the initial processing of raw picture data to correct for geometric distortion or to calibrate the data radiometrically, followed by the removal of any noise that may have already existed in the data. Data is imaged using the second category to effectively present it for further visual interpretation (Lillesand et al., 2015). It comprises a variety of methods for improving the visual contrast between scene elements (Maarez et al., 2022). The third category focuses on converting quantitative strategies for recognizing scene elements from visual analysis of the image data (Lu & Weng, 2007).

The ability to recognize and assess environmental changes depends on sensors that can produce calibrated (known exactness and precision) and foreseen estimates of the surface of Earth's sections throughout time (Jaber et al., 2022). On the other hand, the ability to distinguish between product artefacts and changes in the Earth's processes being watched is crucial for the accurate interpretation of the information collected from the global and remote-detecting items. Therefore, radiometric calibration is crucial for obtaining high-quality information and, as a result, more downstream goods (Hasan et al., 2021).

Moreover, radiometric calibration describes the perfect (absolute) calibration method of TerraSAR-X (TSX) data. Thus, the absolute calibration method takes into consideration all the changes in the radiometric values which are independent of characteristics of the target (Schwerdt et al., 2008). This property will allow to reduce the variance in the image radiometry and to make the TSX system

(which is produce from differences in angles of incidence, geometry of ascending –descending) more easily in comparable as well as more compatible by using other sensors of the radar (Breit et al., 2009). The research aims to study the effect of noise equivalent beta on TerraSAR-X radar images through the backscattering coefficient and the extent of its impact on the classification of features in the images.

2. Material and methods

2.1. TerraSAR-X

In June 2007, the new German synthetic aperture radar (SAR) TerraSAR-X was unveiled, with a 5-year planned lifespan (Buckreuss et al., 2008). The satellite's design is based on sound scientific research and understanding gleaned from the productive Synthetic Aperture Radar SIR-C/X-SAR and SRTM missions (Dibs et al., 2022). It includes a high frequency X-band SAR sensor that may be used in a variety of imaging modes to satisfy the needs of various applications. This satellite is collecting data in the three primary imaging modes, including the Spotlight, Strip map, and Scan-SAR modes, all of which have excellent resolution, a high capacity for detail analysis, and huge data swaths for greater coverage (Schwerdt et al., 2007). The satellite considers the first available radar satellite which is independent of cloud and produce 1 meter to 16 meter resolutions (Moreira et al., 2021).

2.2. Strip map Mode

Strip map Mode (SM) is the type of TSX mode is a basic SAR imaging mode and other types of sensors. The continuous sequence principal of radar pulses is depended to illuminate the ground swath. In addition, the antenna beam in this mode is directed to a fixed angle in elevation and azimuth. Consequently, this leads to an image strip and constant image quality in azimuth. The configuration geometry of SM mode geometry is showed in reference (Schwerdt et al., 2007).

2.3. Noise Equivalent Beta Naught (NEBN) estimation

2.3.1. Description and method of estimation NEBN

Noise Equivalent Beta Naught is the different noise influence that beneficence to the radar signal (Naught & Naught, 2014). Typically, the TSX data shipping package annotation file will note this kind of noise, specifically in the section noise and expressed in forms of scaled polynomial with calibration factor K_s (Buckreuss et al., 2018). It should be mentioned, the noise power is described by those polynomials as a function of the main range noise contributing elements, such as elevation antenna pattern, transmitted energy, and noise receiver (Buckreuss et al., 2018). On the other hand, in TSX data files, section noise and time are both used to express the noise, which is computed at specified azimuth time tags and is a function of range time. Moreover, the polynomial parameters can be extracted from section of image noise in annotated TSX file. These parameters of polynomial are mainly defining by two parameters: the first is <time UTC>, referring to the azimuth time (sensor flight track) that the noise estimation is made. The second parameters of polynomial is the <noise Estimation> which includes the following parameters (Gregorek et al., 2019):

(1) Validity Range Min and validity Range Max that define the validity range of the computed polynomial, (2) Reference Point, (3) Polynomial Degree defines the degree of the polynomial computed for the noise description (4) the polynomial coefficient (Naught & Naught, 2014). Depending on the previous parameters the polynomial

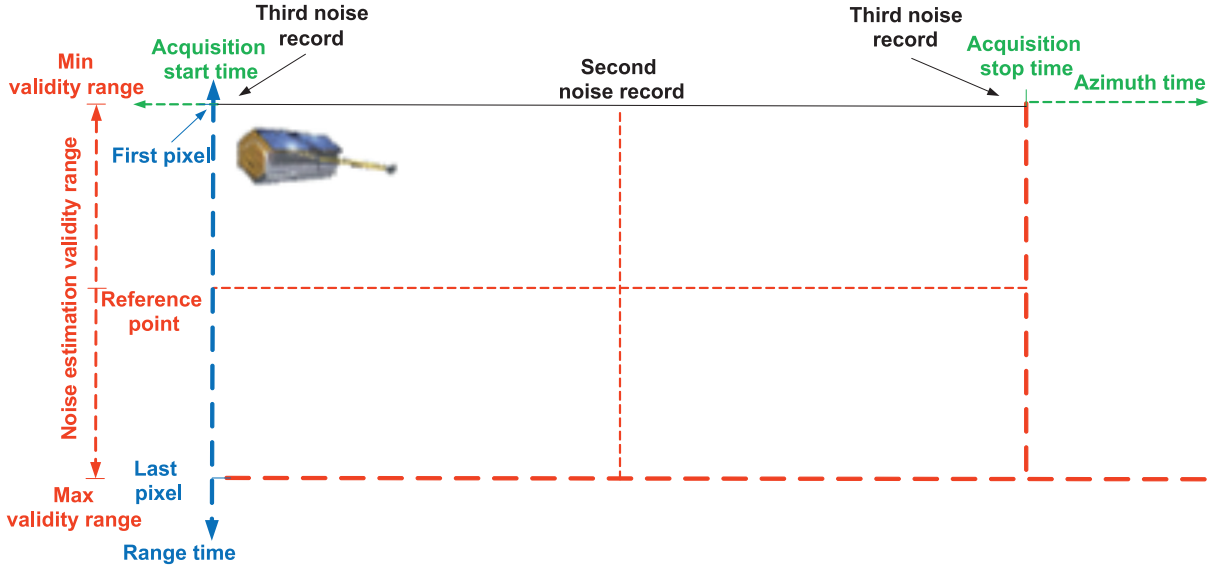

Figure 1. Noise estimation configuration

noise or NEBN can be calculated using Equation (4):

$$NEBN = K_s . \sum_{i=0}^{\deg} coeff_i . \left(\tau - \tau_{ref}\right)^i ; \quad (1)$$

$$\tau = \left|\tau_{\min}, \tau_{\max}\right|,$$

where K_s is the calibration factor; $\deg$ is polynomial degree; $coeff_i$ is coefficient exponent; τ_{ref} is reference Point and $\tau_{\min}, \tau_{\max}$ are validity Range Min and validity Range Max, respectively.

2.3.2. Noise estimation configuration

The general configuration of the NEBN records can be depicted in Figure 1. The configuration of noise is significantly consisting of many parameters such as start time and stop time of the acquisition of the satellite in addition to the parameters that mentioned previously (Balss et al., 2009). The first and last noise records, however, are corresponding to the acquisition start and stop periods, respectively (Breit et al., 2009). The period of the acquisition in range further defines each noise estimation validity range.

Therefore, the extraction of NEBN parameters have been extracted depending on the data that provided by data image as shown in Figure 2, which shows different noise estimation. For each noise estimate, the validity Range Min, validity Range Max, reference Point, polynomial Degree, and coefficient exponent are provided. In the instance of the dataset under consideration, the noise has been estimated five times.

Figure 2. Image noise section and noise estimation

In our case the NEBN has been estimated of TSX strip map in polarization VV and HH after extraction all the information and the parameters of the satellite system.

2.3.3. Calculation of Sigma Naught

The scattering coefficient, often known as sigma nought, is the average reflectivity of a horizontal material sample normalized with regard to a unit area on the ground plane (Mittermayer et al., 2013). The ratio of dispersed wave density to incident wave density from the surface defines sigma nought, a dimensionless metric. It is dependent upon the frequency, polarizations, and orientations of the incident and scattered waves. The backscattering reflected off a target is further influenced by the relative orientation of the lighted resolution cell and the sensor, as well as the space between them. In order to calculate Sigma Naught, a complete understanding of the local slope, also known as the local incidence angle (Yang & Jeong, 2018), as indicated by Equation (2):

$$\sigma^0 = \left(k_s . \left|DN\right|^2 - NEBN\right) . \sin\theta_{loc}, \quad (2)$$

where k_s is a scaling factor of calibration and processor provided with image data in the annotated file; *DN* is the intensity values of pixel; *NEBN* it considers the impact of various types of noise to receive the signal and is the Noise Equivalent Beta Naught (Shareef et al., 2015); θ_{loc} is the angle of local incidence.

3. Result and discussion

3.1. NEBN estimation of TerraSAR-X polarization VV

NEBN is considered one of the influences that effect on the radar signal. It is depending on the considered application without specifying the type of the application. From this reason, it was very necessary to know the values and a range of this noise in our TSX data.

In this instance, the data from the suggested xml file is used to compute NEBN. In our images, the degree of the considered polynomial is 7, according to Equation (2), the degree of polynomial composes the noise. The general equation of the noise will be modified depending the polynomial degree therefore the produce Equation given as (3).

$$NEBN = K_s . \sum_{i=0}^{\deg} coeff_0 . \left(\tau - \tau_{ref}\right)^0 + coeff_1 . \left(\tau - \tau_{ref}\right)^1 + coeff_2 . \left(\tau - \tau_{ref}\right)^2 + coeff_3 . \left(\tau - \tau_{ref}\right)^3 + coeff_4 . \left(\tau - \tau_{ref}\right)^4 + coeff_5 . \left(\tau - \tau_{ref}\right)^5 + coeff_6 . \left(\tau - \tau_{ref}\right)^6 + coeff_7 . \left(\tau - \tau_{ref}\right)^7 ; \quad (3)$$

$$\tau = \left|\tau_{\min}, \tau_{\max}\right|.$$

The parameters needed for NEBN estimate have the following values:

$\tau_{\min}$ = 3.92576227697988452E-03;

$\tau_{\max}$ = 3.98390732387753251E-03;

τ_{ref} = 3.95483480042870851E-03.

TSX SM has five-time acquisition as shown in Table 1. For this reason, each time is corresponding on the polynomial coefficient consequently is produced five noise equivalents. That means the noise of the satellite system is generated while the satellite is captured the image.

The evolution of the NEBN contributions is depicted in Figures 3 and 4, according to various range time values (maximum, minimum, and average). The black solid line depicts the NEBN variation for the initial noise estimation.

Table 1. Polynomial coefficients for 5 times

coeffs	Time1	Time2	Time3
coeff0	5.15878309843634042E+02	5.15797387388483685E+02	5.15627338517567523E+02
coeff1	9.24907811619396787E+05	8.86152208822926506E+05	8.46226050115001621E+05
coeff2	2.94614568211325317E+11	2.94271428321358215E+11	2.94040041941162109E+11
coeff3	–4.26018677834681750E+14	–4.25986429811684688E+14	–4.22330213052153250E+14
coeff4	9.38504867633009787E+19	9.42387655647560827E+19	9.42605310634792223E+19
coeff5	1.12107571321444420E+24	1.06271985911092123E+24	1.01403544852052863E+24
coeff6	3.33847234473255634E+28	3.33207452580676125E+28	3.35429664515785607E+28
coeff7	–4.88757156091361862E+32	–4.82305346075453O7E+32	–4.71354503262673221E+32
coeffs	Time4	Time5	
coeff0	5.15560999364576901E+02	5.15444685633192194E+02	
coeff1	7.91157618505412247E+05	6.97840922494747909E+05	
coeff2	2.94220228128106262E+11	2.94992604965920349E+11	
coeff3	–4.30163992255194000E+14	–4.73150736505679938E+14	
coeff4	9.38386613590899261E+19	9.28249582345225503E+19	
coeff5	9.62293016826081677E+23	8.84334120488658662E+23	
coeff6	3.39212790442823279E+28	3.41827209180219971E+28	
coeff7	–4.55441993457744486E+32	–4.33909913813689005E+32	

Table 2. NEBN estimation in TSX strip map SAR-VV at various times and with various coefficients image

	$\tau = \tau_{min}$	$\tau = \tau_{max}$	$\tau = \tau_{ref}$
$\tau = \tau_{ref}$	$\tau_{min} = \tau_{ref}$	$\tau_{max} = \tau_{ref}$	$\tau_{ref} = \tau_{ref}$
	–2.9073e-05	2.9073e-05	0
NEBN1	*ks* × 820.9680 = 0.01022	*ks* × 883.2178 = 0.0109	*ks* × 515.8783 = 0.0064
NEBNdB1	–19.9046	–19.5872	–21.9224
NEBN2	*ks* × 832.3168 = 0.01036	*ks* × 880.8610 = 0.0109	*ks* × 515.7973 = 0.0064
NEBNdB2	–19.8449	–19.5988	–21.9230
NEBN3	*ks* × 824.7344 = 0.0102	*ks* × 878.7553 = 0.0109	*ks* × 515.6273 = 0.0064
NEBNdB3	–19.8847	–19.6092	–21.9245
NEBN4	*ks* × 827.3362 = 0.0103	*ks* × 876.1795 = 0.0109	*ks* × 515.5609 = 0.0064
NEBNdB4	–19.8710	–19.6219	–21.92508
NEBN5	*ks* × 832.3168 = 0.01036	*ks* × 871.1393 = 0.0108	*ks* × 515.4446 = 0.0064
NEBNdB5	–19.8449	–19.6470	–21.9260

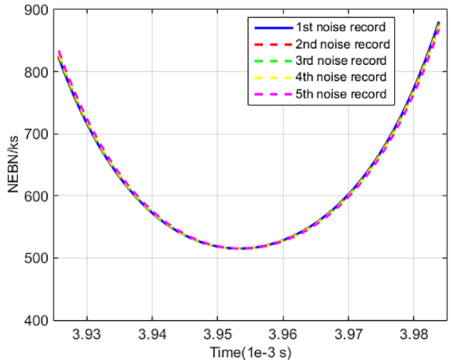

Figure 3. At the three time tags, noise contribution is in azimuth (real values)

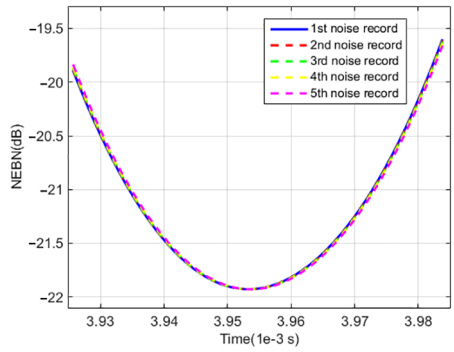

Figure 4. At the three time tags, noise contribution is in azimuth (dB values)

The green dot-dash lines and the orange dash lines, respectively, show the evolution of NENB for the second and last record noise.

In the figures above the noise have been estimated in linear and decibel, to make us an indication about the noise that taken during the capture images via satellite. As a result, from TSX strip map with polarization VV, five noise equivalents have been produced. The noise variance depends on the minimum, maximum and reference time of the satellite. In all cases, the depending on the reference tau time record the smallest noise, while depending on the maximum tau time is recorded a noise the highest values of the noise in VV polarization strip map. Thus, the maximum NEBN is equalled to –19.872 dB in the first NEBN when the $\tau = \tau_{max}$. In the other hand, the minimum NEBN is equalled to –21.960 dB in case of $\tau = \tau_{ref}$ as shown in Table 2.

3.1.1. NEBN estimation of TSX images with polarization HH

For all TerraSAR-X products, the same noise estimation process should be used (all imaging modes and polarization channels). Typically, the noise is estimated at several specified time tags as shown in Table 3 and Table 4. Linear interpolation can be used to assess the noise at the required time if the NEBN value is required at a time when it has not yet been assessed.

The evolution of the NEBN contributions is depicted in Figures 5 and 6, according to various range time values (max, min, etc.). The black solid line depicts the NEBN

Table 3. Polynomial coefficients for 5 times HH

coeffs	Time1	Time2	Time3
coeff0	4.95672765266756244E+02	4.95579548697977259E+02	4.95400445538920906E+02
coeff1	1.13433841545603471E+06	1.09561533342393558E+06	1.05581293202039669E+06
coeff2	2.93348152735565979E+11	2.93007042769659363E+11	2.92776582403344910E+11
coeff3	3.79465650602268812E+14	–3.79125067034813625E+14	–3.75752645276631812E+14
coeff4	9.27328901090093793E+19	9.31503935093545861E+19	9.32127611973567447E+19
coeff5	9.44591238950333079E+23	8.86952739943372879E+23	8.39605622657173349E+23
coeff6	3.34757970572534728E+28	3.34157629544508113E+28	3.36280846350911151E+28
coeff7	4.61721039307288724E+32	–4.55899127554145480E+32	–4.45798964828396372E+32
coeffs	Time4	Time5	
coeff0	4.95315345983313023E+02	4.95167952065005181E+02	
coeff1	1.00117322844753624E+06	9.08722657142369775E+05	
coeff2	2.92947041866876831E+11	2.93685485005250549E+11	
coeff3	–3.84542900195858812E+14	–4.29240304483436875E+14	
coeff4	9.28668477806595768E+19	9.20017721729507328E+19	
coeff5	7.90030312914111691E+23	7.15482183216229910E+23	
coeff6	3.39833072711056314E+28	3.42113592761200204E+28	
coeff7	–4.31015076608480375E+32	–4.10983851643606517E+32	

Table 4. NEBN estimation at different time and different coefficients in TerraSAR-X strip map HH image

	$\tau = \tau_{min}$	$\tau = \tau_{max}$	$\tau = \tau_{ref}$
$\tau = \tau_{ref}$	$\tau_{min} = \tau_{ref}$	$\tau_{max} = \tau_{ref}$	$\tau_{ref} = \tau_{ref}$
	–2.9073e-05	2.9073e-05	0
NEBN1	*ks* × 760.0479 = 0.0095	*ks* × 900.0994 = 0.0112	*ks* × 495.6728 = 0.0062
NEBNdB1	–20.2395	–19.5050	–22.0959
NEBN2	*ks* × 796.9997 = 0.0099	*ks* × 862.9085 = 0.0107	*ks* × 495.5795 = 0.0062
NEBNdB2	–20.0333	–19.6882	–22.0967
NEBN3	*ks* × 798.6789 = 0.0099	*ks* × 860.8271 = 0.0107	*ks* × 495.4004 = 0.0062
NEBNdB3	–20.0242	–19.6987	–22.0983
NEBN4	*ks* × 801.2799 = 0.0100	*ks* × 858.2788 = 0.0107	*ks* × 495.3153 = 0.0062
NEBNdB4	–20.0100	–19.7116	–22.0991
NEBN5	*ks* × 806.2591 = 0.0100	*ks* × 853.2925 = 0.0106	*ks* × 495.1680 = 0.0062
NEBNdB5	–19.9831	–19.7369	–22.1004

variation for the initial noise estimation. The progression of NENB for the second and recorded the last noise, respectively, was explained by the orange dash line and the green dot-dash lines as shown in Figures 5 and 6.

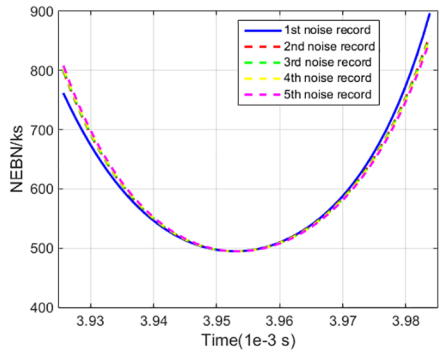

Figure 5. At the three time tags, noise contribution is in azimuth (real values)

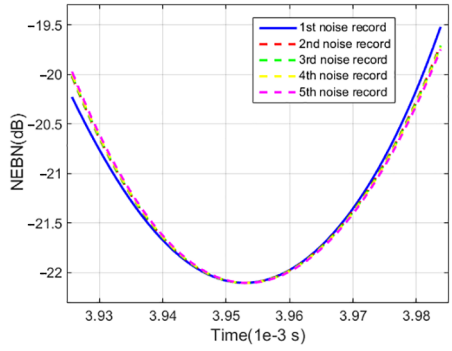

Figure 6. At the three time tags, noise contribution is in azimuth (dB values)

The same result has been recorded when we analysed the noise concerned to HH polarization. However, the higher noise was in maximum tau time. In the other hand, the smallest noise was in reference point in linear and dB values. The behaviour of the noise in linear values is a same comparing of dB value as shown in the radiometric index. Thus, the maximum NEBN in HH polarization is found equal to –19.5050 dB in the first NEBN when the $\tau = \tau_{max}$. In the other hand, the minimum NEBN is equaled to –22.1004 dB when $\tau = \tau_{ref}$. The value in Figure 6 shows the polynomial values relative to the noise time.

3.1.2. Influence of (NEBN) on backscattering coefficient of TSX

Sigma naught (σ^0) or backscattering coefficient represents the main important things in our works. The backscattering coefficient is calculated in different ways depending on the noise effect. In general, the Calculation of backscattering confidents here is mainly depending on the many parameters such incident angle, noises as well as the properties of the surfaces. In this work, the incident angle of the acquired images is constant in Horizontal and vertical polarization. In the other hand, supposing the properties of the surfaces or any additional condition is included in the calibration factor of the TSX. Therefore, the backscattering coefficients are calculated once, depending on the obtained values from the previous section and once again, in case of its neglected.

The NEBN is produced for each noise time in linear form in HH and VV polarizations. That means there is a noise for each time during the images is captured. The mean of each noise is representing in Table 5.

The total mean of the NEBN for HH is equal to 0.007440379328700 and for VV is equal to 0.007699096310979. According to the Equation (3), the values of the NEBN will be subtracted from each value of Beta that is derived directly from pixel values.

Figure 7 shows the backscattering coefficients of the TSX images in different polarization. The obtained backscattering is generally containing the noise.

Figure shows the computed backscattering coefficient for HH and VV polarization from the TSX image. For the linear backscattering coefficients as shown in Figures 8a and 8b is obtained by using the Equation (3) in previous sections. This equation is mainly supposing that the NEBN is ignored from the calculations and thus, there is no effect of this noise on the general backscattering coefficient. In the other hand, the Equation (3) is presented another form to measure the backscattering coefficient as shown in Figures 8c and 8d.

The visual interpretation of sigma σ^0 which is result from the comparison between existence case and absence case (in the other word: with and without noise) of the noise illustrated that there is no different between them. In the other hand, for more details and more precise, an example of small images is used to show the values of obtained backscattering.

Table 5. Mean value of calculated NEBN for TSX images (HH, VV)

TSX image, HH polarization		TSX image, VV polarization	
NEBN	Mean value (linear)	NEBN	Mean value
NEBN(1)	0.007442644191940	NEBN(1)	0.007702065831033
NEBN(2)	0.007442183602661	NEBN(2)	0.007700546963490
NEBN(3)	0.007439546976829	NEBN(3)	0.007697955106599
NEBN(4)	0.007438948095810	NEBN(4)	0.007697509280454
NEBN(5)	0.007438573776261	NEBN(5)	0.007697404373321

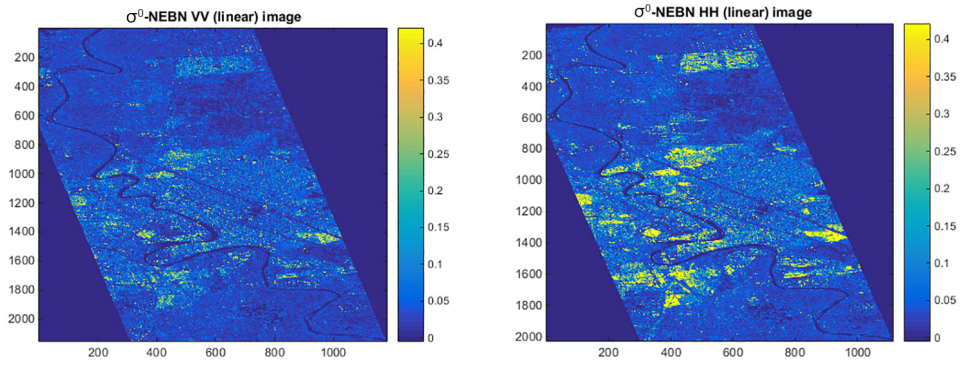

a) σ^0 in linear unit for polarization VV

b) σ^0 in linear for polarization HH

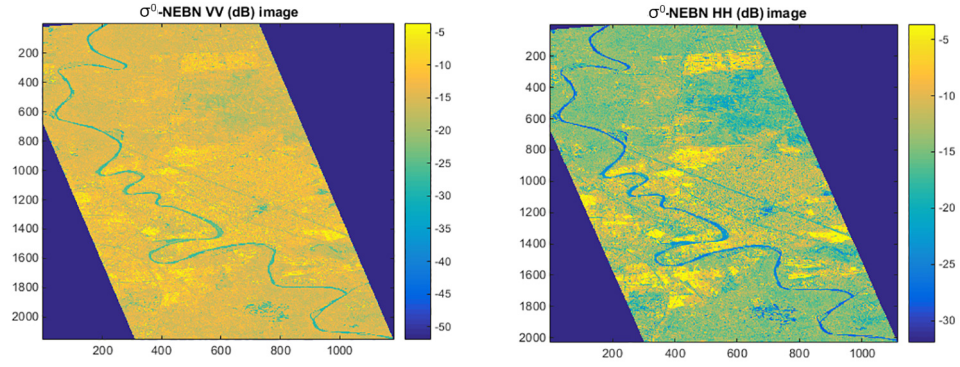

c) σ^0 in dB for polarization VV

d) σ^0 in dB for polarization HH

Figure 7. Sigma for TSX images contains NEBN for HH and VV polarization in different measured units

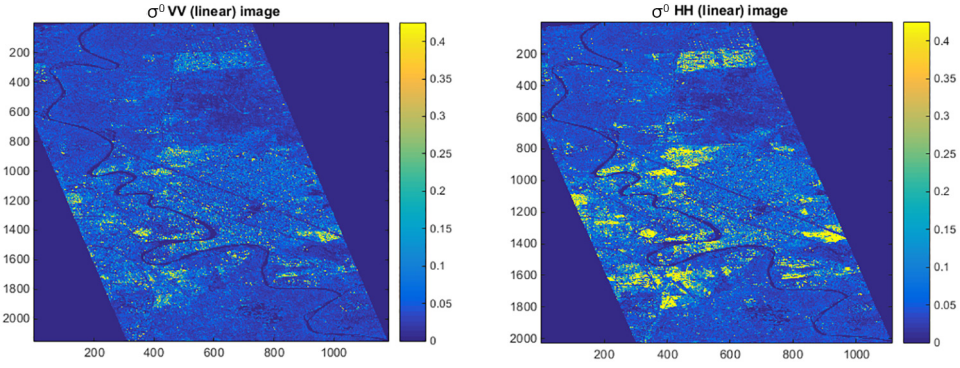

a) σ^0 in linear unit for polarization VV

b) σ^0 in linear for polarization HH

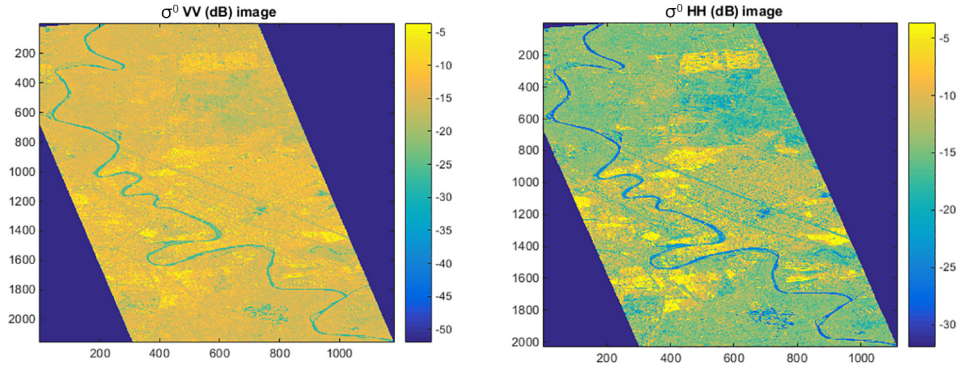

c) σ^0 in dB for polarization VV

d) σ^0 in dB for polarization HH

Figure 8. σ^0 for TSX images for HH and VV polarization in different measured units

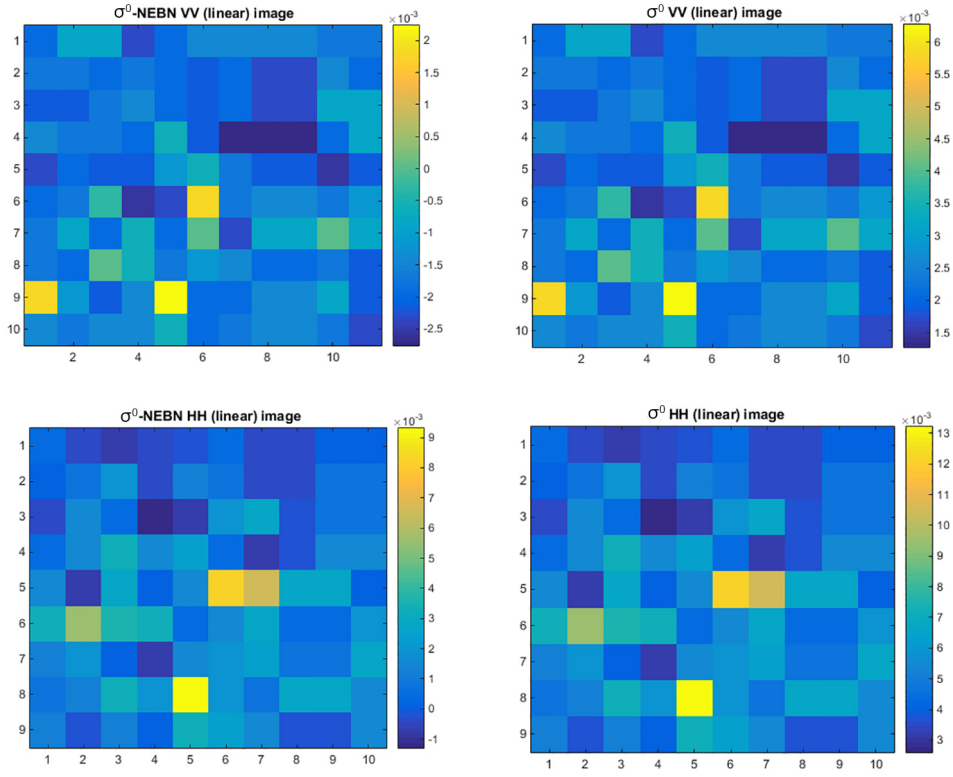

Figure 9. σ^0 values for a water body sample in two polarization (HH, VV)

The Figure 9 shows the backscattering values with and without NEBN. Because of our subject is concerned directly with water body properties. It was very necessary to take an example to study the influences of the noise and their effect on the reflected sigma. Thus, the result is demonstrated that the NEBN plays the main roles in decreasing the values of backscattering coefficient in TSX image. The influence of this noise is usually high in water body surface, because this surface is generally having small backscattering coefficients compared with other land cover.

Moreover, the strong value of found for images acquired in Strip-map mode did not allow a calibration of many pixels because the term $k_s DN^2$ is lower than the noise NBEN.

4. Conclusions

The radiometric calibration and calculation process of the backscattering coefficients and reflectance in radar SAR images and optical images. Each type of the satellite data has a calibration method differs from another taking into account the satellite type and application purpose. In the TerraSAR-X images the effect of NEBN is studied relative to the calculated backscattering coefficient. Thus, the detecting of the NEBN helped to reduce the backscattering values making them in somewhat unreasonable.

On the other hand, when computations in dB are required, the presence of the NEBN in satellite photos will make backscattering confident in complicated values. In the radiometric appendix, several polarizations of TSX images show calculated values of backscattering coefficients. It should be noted that for each calculated mean NEBN, we used the total mean of NEBN, which represents the entire mean. As a result, finding the sigma noise equivalent of sigma zero assisted in lowering the backscattering values and bringing them closer to normal, which negated the impact of noise on classification.

References

Balss, U., Breit, H., & Fritz, T. (2009). Noise-related radiometric correction in the TerraSAR-X multimode SAR processor. *IEEE Transactions on Geoscience and Remote Sensing*, *48*(2), 741–750. https://doi.org/10.1109/TGRS.2009.2035443

Breit, H., Fritz, T., Balss, U., Lachaise, M., Niedermeier, A., & Vonavka, M. (2009). TerraSAR-X SAR processing and products. *IEEE Transactions on Geoscience and Remote Sensing*, *48*(2), 727–740. https://doi.org/10.1109/TGRS.2009.2035497

Buckreuss, S., Schättler, B., Fritz, T., Mittermayer, J., Kahle, R., Maurer, E., Böer, J., Bachmann, M., Mrowka, F., Schwarz, E., Breit, H., & Steinbrecher, U. (2018). Ten years of TerraSAR-X operations. *Remote Sensing*, *10*(6), Article 873. https://doi.org/10.3390/rs10060873

Buckreuss, S., Werninghaus, R., & Pitz, W. (2008). The German satellite mission TerraSAR-X. In *2008 IEEE Radar Conference* (pp. 1–5). IEEE. https://doi.org/10.1109/RADAR.2008.4720788

Dibs, H., Hasab, H. A., Jaber, H. S., & Al-Ansari, N. (2022). Automatic feature extraction and matching modelling for highly noise near-equatorial satellite images. *Innovative Infrastructure Solutions*, *7*(1), 1–14. https://doi.org/10.1007/s41062-021-00598-7

Gregorek, D., Günzel, D., Rust, J., Paul, S., Velotto, D., Imber, J., Tings, B., & Frost, A. (2019). FPGA prototyping of a high-resolution TerraSAR-X image processor for iceberg detection. In *2019 53rd Asilomar Conference on Signals, Systems, and Computers* (pp. 1832–1835). IEEE. https://doi.org/10.1109/IEEECONF44664.2019.9048985

Hasan, S. F., Shareef, M. A., & Hassan, N. D. (2021). Speckle filtering impact on land use/land cover classification area using the combination of Sentinel-1A and Sentinel-2B (a case study of Kirkuk city, Iraq). *Arabian Journal of Geosiences*, *14*(4), Article 276. https://doi.org/10.1007/s12517-021-06494-9

Jaber, H. S., Shareef, M. A., & Merzah, Z. F. (2022). Object-based approaches for land use-land cover classification using high resolution quick bird satellite imagery (a case study: Kerbela, Iraq). *Geodesy and Cartography*, *48*(2), 85–91. https://doi.org/10.3846/gac.2022.14453

Lillesand, T., Kiefer, R. W., & Chipman, J. (2015). *Remote sensing and image interpretation*. John Wiley & Sons.

Lu, D., & Weng, Q. (2007). A survey of image classification methods and techniques for improving classification performance. *International Journal of Remote Sensing*, *28*(5), 823–870. https://doi.org/10.1080/01431160600746456

Maarez, H. G., Jaber, H. S., & Shareef, M. A. (2022). Utilization of Geographic Information System for hydrological analyses: A case study of Karbala province, Iraq. *Iraqi Journal of Science*, *63*(9), 4118–4130. https://doi.org/10.24996/ijs.2022.63.9.39

Mittermayer, J., Wollstadt, S., Prats-Iraola, P., & Scheiber, R. (2013). The TerraSAR-X staring spotlight mode concept. *IEEE Transactions on Geoscience and Remote Sensing, 52*(6), 3695–3706. https://doi.org/10.1109/TGRS.2013.2274821

Mohammed Noori, A., Falih Hasan, S., Mahmood Ajaj, Q., Ridha Mezaal, M., Z. M. Shafri, H., & Aidi Shareef, M. (2018). Fusion of airborne hyperspectral and WorldView2 multispectral images for detailed urban land cover classification a case study of Kuala Lumpur, Malaysia. *International Journal of Engineering & Technology*, *7*(4.37), 202–206. https://doi.org/10.14419/ijet.v7i4.37.24102

Moreira, A., Zink, M., Bartusch, M., Quiroz, A. E. N., & Stettner, S. (2021). German spaceborne SAR missions. In *2021 IEEE Radar Conference (RadarConf21)* (pp. 1–6). IEEE. https://doi.org/10.1109/RadarConf2147009.2021.9455326

Naught, B., & Naught, S. (2014). *Radiometric calibration of TerraSAR-X data*. Airbus Defence & Space.

Rasti, B., Chang, Y., Dalsasso, E., Denis, L., & Ghamisi, P. (2022). Image restoration for remote sensing: Overview and toolbox. *IEEE Geoscience and Remote Sensing Magazine, 10*(2), 201–230. https://doi.org/10.1109/MGRS.2021.3121761

Schwerdt, M., Brautigam, B., Bachmann, M., & Doring, B. (2007). TerraSAR-X calibration-first results. In *2007 IEEE International Geoscience and Remote Sensing Symposium* (pp. 3932–3935). IEEE. https://doi.org/10.1109/IGARSS.2007.4423705

Schwerdt, M., Bräutigam, B., Bachmann, M., & Döring, B. (2008). TerraSAR-X calibration results. In *7th European Conference on Synthetic Aperture Radar* (pp. 1–4). VDE. https://doi.org/10.1109/IGARSS.2008.4778963

Shareef, M. A., Toumi, A., & Khenchaf, A. (2015). Estimation and characterization of physical and inorganic chemical indicators of water quality by using SAR images. In *Proceedings of SPIE, SAR Image Analysis, Modeling, and Techniques XV* (Vol. 9642, pp. 140–150). SPIE. https://doi.org/10.1117/12.2194503

Yang, D., & Jeong, H. (2018). Verification of Kompsat-5 sigma naught equation. *Korean Journal of Remote Sensing*, *34*(6_3), 1457–1468.